SANDIA REPORT
SAND2008-6161
Unlimited Release
Printed September 2008

Volumetric Plasma Source Development and Characterization

Mark D. Johnston, Kelly Hahn, Bryan V. Oliver, Thomas A. Mehlhorn,
Darryl W. Droemer, Robert L. Starbird, Marlon D. Crain, Yitzhak Maron

Prepared by
Sandia National Laboratories
Albuquerque, New Mexico 87185 and Livermore, California 94550

Sandia is a multiprogram laboratory operated by Sandia Corporation,
a Lockheed Martin Company, for the United States Department of Energy's
National Nuclear Security Administration under Contract DE-AC04-94AL85000.

Issued by Sandia National Laboratories, operated for the United States Department of Energy by Sandia Corporation.

Available to DOE and DOE contractors from
U.S. Department of Energy
Office of Scientific and Technical Information
P.O. Box 62
Oak Ridge, TN 37831

Telephone: (865) 576-8401
Facsimile: (865) 576-5728
E-Mail: reports@adonis.osti.gov
Online ordering: http://www.osti.gov/bridge

Available to the public from
U.S. Department of Commerce
National Technical Information Service
5285 Port Royal Rd.
Springfield, VA 22161

Telephone: (800) 553-6847
Facsimile: (703) 605-6900
E-Mail: orders@ntis.fedworld.gov
Online order: http://www.ntis.gov/help/ordermethods.asp?loc=7-4-0#online

SAND2008-6161
Unlimited Release
Printed September 2008

Volumetric Plasma Source Development and Characterization

Mark D. Johnston[1], Kelly Hahn, Bryan V. Oliver, and Thomas A. Mehlhorn
Advanced Radiographic Technologies Department
Sandia National Laboratories
P.O. Box 5800
Albuquerque, New Mexico 87185-1195

Darryl W. Droemer, Marlon D. Crain, and Robert L. Starbird
National Security Technologies, LLC
P.O. Box 98521
Las Vegas, NV 89193

Yitzhak Maron
Weizmann Institute of Science
Rehovot, Israel 76100

Abstract

The development of plasma sources with densities and temperatures in the 10^{15}-10^{17} cm^{-3} and 1-10eV ranges which are slowly varying over several hundreds of nanoseconds within several cubic centimeter volumes is of interest for applications such as intense electron beam focusing as part of the x-ray radiography program. In particular, theoretical work [1,2] suggests that replacing neutral gas in electron beam focusing cells with highly conductive, pre-ionized plasma increases the time-averaged e-beam intensity on target, resulting in brighter x-ray sources. This LDRD project was an attempt to generate such a plasma source from fine metal wires. A high voltage (20-60kV), high current (12-45kA) capacitive discharge was sent through a 100μm diameter aluminum wire forming a plasma. The plasma's expansion was measured in time and space using spectroscopic techniques. Lineshapes and intensities from various plasma species were used to determine electron and ion densities and temperatures. Electron densities from the mid-10^{15} to mid-10^{16} cm^{-3} were generated with corresponding electron temperatures of between 1 and 10eV. These parameters were measured at distances of up to 1.85 cm from the wire surface at times in excess of 1μs from the initial wire breakdown event. In addition, a hydrocarbon plasma from surface contaminants on the wire was also measured. Control of these contaminants by judicious choice of wire material, size, and/or surface coating allows for the ability to generate plasmas with similar density and temperature to those given above, but with lower atomic masses.

[1]Email: mdjohn@sandia.gov

Acknowledgements

Sandia is a multiprogram laboratory operated by Sandia Corporation, a Lockheed-Martin company, for the United States Department of Energy's National Nuclear Security Administration, under contract DE-AC04-94AL85000.

Table of Contents

List of Figures

List of Tables

I. Introduction

A series of experiments were conducted to measure the plasma parameters associated with the breakdown of a 100μm diameter aluminum wire by means of a capacitive discharge. The motivation for this work was to create a volumetric plasma source (several cubic centimeters) with plasma densities and temperatures in the 10^{15}-10^{17} cm^{-3} and 1-10eV ranges which are slowly varying over several hundreds of nanoseconds for applications such as intense electron beam focusing for x-ray radiography. In one radiographic configuration, relativistic electron beams are transported and focused inside neutral gas cells onto high atomic number solid targets (ex. tantalum) to produce bremsstrahlung x-rays for radiographic applications. Within the gas-transport cell, transient ionizations have been shown computationally to limit focal intensity and duration [3]. Time-varying net currents affect the focus of the electron beam and result in focal sweeping which leads to decreased focal intensity and larger average radiation spot sizes. Future x-ray source requirements require a three-fold focal intensity increase. To achieve this, recent work [1,2] suggests that replacing the gas with a highly conductive, pre-ionized plasma (~10^{16} cm^{-3} and ~5eV) enhances the time-averaged beam intensity on target. As yet, no viable source has been developed. Based on theoretical calculations for the ablation rates of z-pinch wire arrays [4,5], it is suggested that a properly tailored, over-massed wire array driven with a low current (~100kA), long pulse (~500ns) should produce a stable, on-axis plasma column with densities of ~10^{16} cm^{-3} for a few hundred nanoseconds, which is sufficient for radiographic applications. This LDRD project was the first attempt to generate such a plasma source from fine metal wires and to understand to what degree a volumetric plasma source can be created, controlled, and maintained for several hundreds of nanoseconds. For these initial studies, primarily single wire-single return current geometries were studied and the results are summarized here. For radiographic applications, it is envisioned that a few wires (~ 4-8) would be required to create the desired volumes.

In particular, for these experiments, a high voltage (20-60kV), high current (12-45kA) capacitive discharge was sent through a 100μm diameter aluminum wire forming a plasma. The plasma's expansion was measured in time and space using advanced spectroscopic techniques. Lineshapes and intensities from various plasma species were used to determine electron and ion densities and temperatures. Electron densities and temperatures were measured at distances of up to 1.85 cm downstream from the wire at times in excess of 1μs from the initial wire breakdown. Hydrocarbon plasmas from surface contaminants on the wire were also measured and characterized.

II. Experimental Configuration

Details of the experimental configuration including the electrical circuit, wire setup, and diagnostics are presented. Figure 1 shows a schematic of the experimental setup. The electrical circuit, including capacitors, charge relays, and spark-gap switch, was submerged in transformer oil to ensure good electrical isolation. For these experiments, three 80nF capacitors were charged in parallel to positive high voltage (20-60kV) by a 100kV Glassman High Voltage, Inc. power supply and discharged through a triggered Maxwell spark-gap switch to ground. The air-filled Maxwell switch was biased by a Maxwell Power Supply (Model 40150-J) and triggered using a Maxwell Trigger Amplifier (Model 4016).

The wire setup was mounted inside a 6 inch diameter 6-port cross vacuum chamber which was pumped by an Alcatel (ACT 200T) turbo pump to base pressures in the range 10^{-5}-10^{-4}torr.

Current was measured using an Ion Physics Corp. (Model CM-1-L) high current transformer. This monitor was located inside the oil tank and measured the current just prior to entrance into the vacuum chamber as shown in Figure 1. Voltage was measured with a North Star Research resistive probe (Model PVM-1). This monitor was also located in the oil tank and measured the voltage at the output of the gas switch. Electrical signals were recorded onto Tektronix 3054B fast 500MHz oscilloscopes. Further processing of the electrical data was performed using commercial software such as IDL and Excel. Typical current and voltage waveforms for a 40kV charging voltage are shown in Figure 2. The system operates as an under-damped RLC circuit with ~ 900ns half-period. The peak current and average peak voltage for this case were 29kA and 23kV, respectively.

The diagnostic layout is shown in Figure 3. Two gated Photek CCD cameras were used to obtain two simultaneous images of the front and side views of the plasma emission light. These orthogonally oriented images were used to help understand the plasma's volumetric expansion and uniformity.

For these experiments, plasma emission light was collected using a lens/fiber system and transported to two spectrographic systems. One system utilized a 0.5 meter Princeton Instruments spectrometer (SpectraPro 2500i) and a Princeton Instruments fast-gated, intensified CCD camera (PI-Max ICCD 1300HB, 25mm Gen III intensifier) to collect time-resolved visible spectra through 5 fibers within a 11x1 fiber array at several spatial locations in the plasma. The second system utilized a single fiber within the 11x1 array coupled into a 1 meter McPherson monochomator (Model 2061) and recorded onto a National Security Technologies (Generation 4) streak camera. This system was capable of continuously recording spectra in time for 2μs at one spatial location.

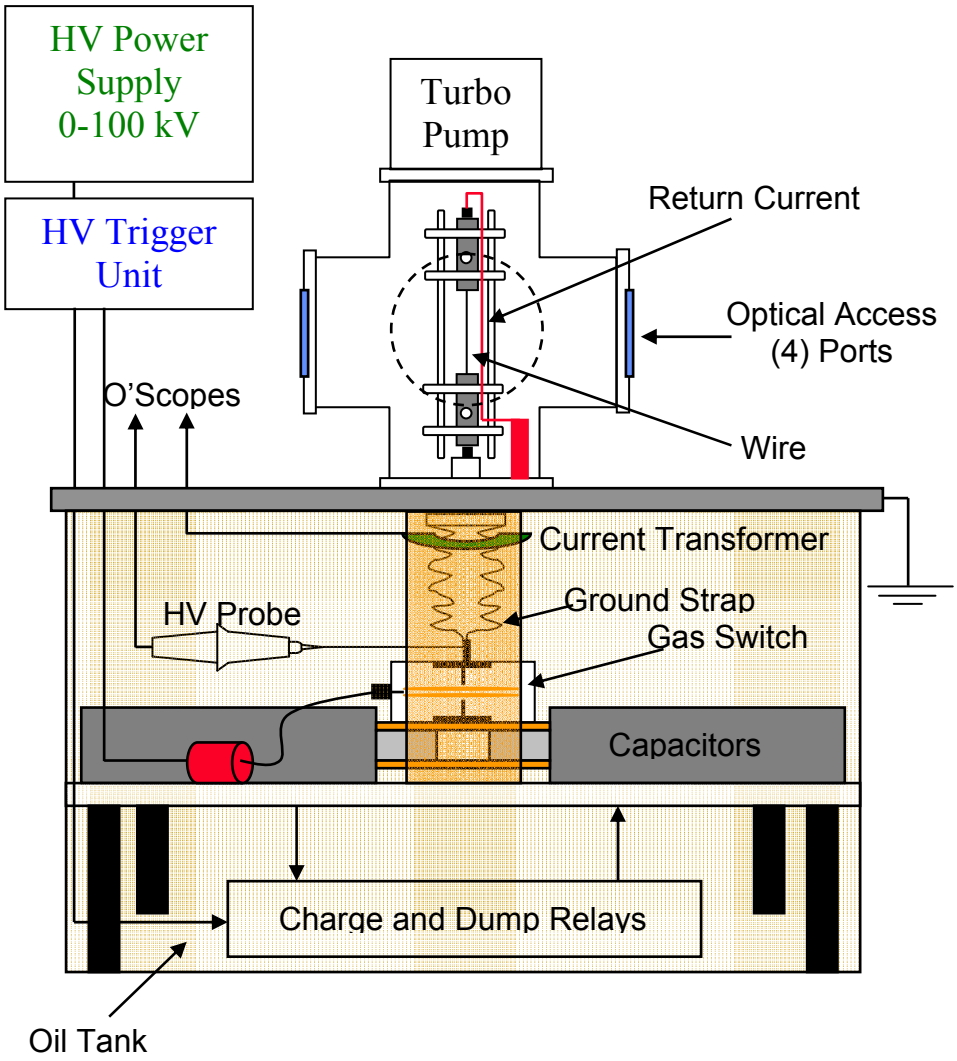

Figure 1. Experimental Setup.

For both spectroscopic measurement systems, the 200μm diameter, 11x1 fused silica linear fiber array was focused through a vacuum window onto the plane of the wire. The individual fibers were focused to a 1.85mm diameter spot which spanned a total radial distance of 18.5mm from the wire surface. As mentioned, the fiber array was split into a one 5x1 linear array and six individual fibers. The 5x1 array was sent to the 0.5 meter spectrograph, a single fiber was sent to the 1m monochromator, and the remaining 5 fibers were sent to individual avalanche photodetectors (APDs). This setup provided both time and spatially resolved spectral measurements of the wire plasma.

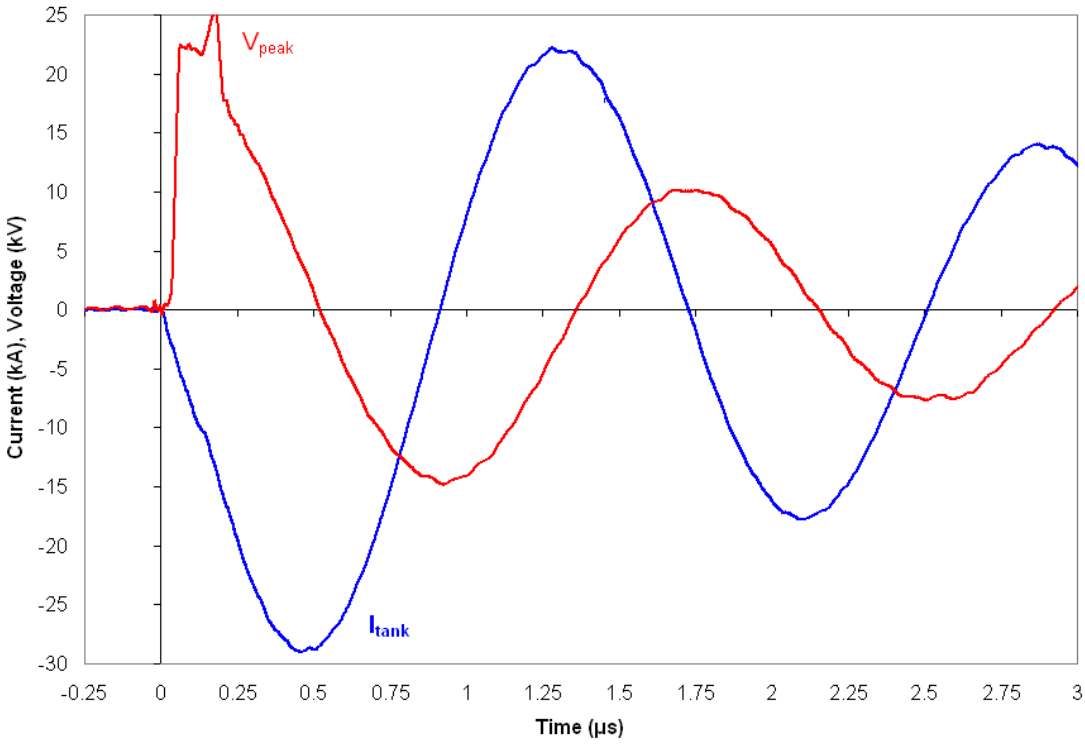

Figure 2. Typical Current and Voltage Trace for 40kV Charging Voltage.

Figure 4 shows the layout of the 11x1 fiber array along with the wire and return current. For each shot, gated spectra were collected at the five radial locations identified by yellow circles (6-10) in Figure 4. In addition, streaked spectra were collected on the farthest downstream fiber labeled A1. The remaining fibers (A2-A6) were sent into avalanche photodetectors (APD's) to monitor the time evolution of the plasma light emission. An unfocused photodetector viewing the entire plasma was located just outside the vacuum chamber.

For experiments presented here, the distance between the top and bottom electrodes was 2cm, the wire was 100µm diameter aluminum (Alfa Aesar, Purtronic), and the return current was positioned 5.5mm downstream of the wire (3.2mm downstream of the electrode holding the wire) as shown in Figure 4. The 12.7mm diameter electrodes were stainless steel and were completely covered with Kapton tape to prevent arcing. The wire was threaded through holes in the Kapton-covered stainless electrodes and made electrical contact by compression between the electrode and stainless steel tapered pins placed through slots in the sides of the rods. The return current made electrical contact with the stainless steel rod and ground (vacuum chamber) via two threaded metal screws.

A second streak camera, also from National Security Technologies (Generation 4), was used to temporally image a 1.45cm cross-section of the plasma light. In this system, plasma light was collected by a lens onto the entrance slit of the streak camera where it was streaked for 2µs. For experiments presented here, the system was aligned to view the

edge of the return current, the wire, and part of the downstream region of the expanding plasma (see Figure 9).

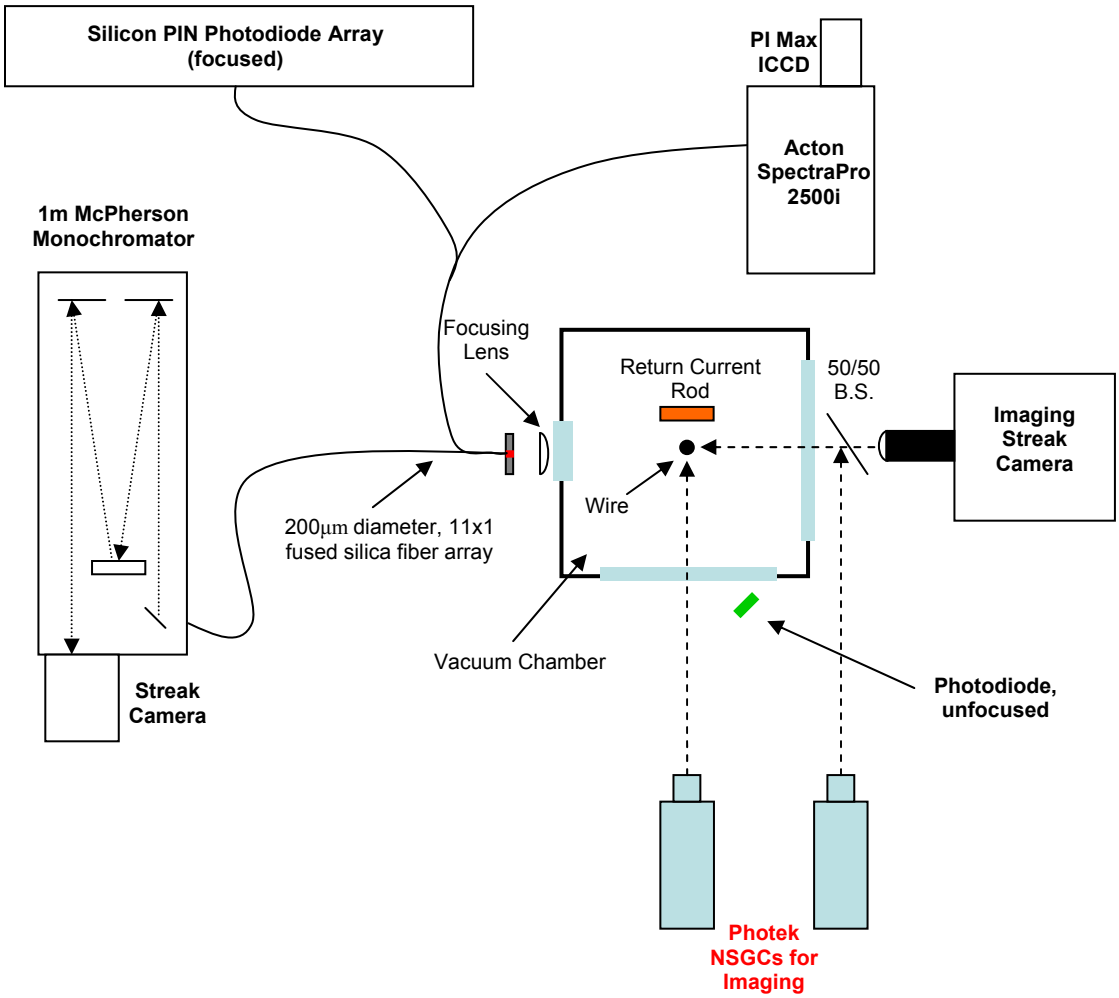

Figure 3. Diagnostic Layout.

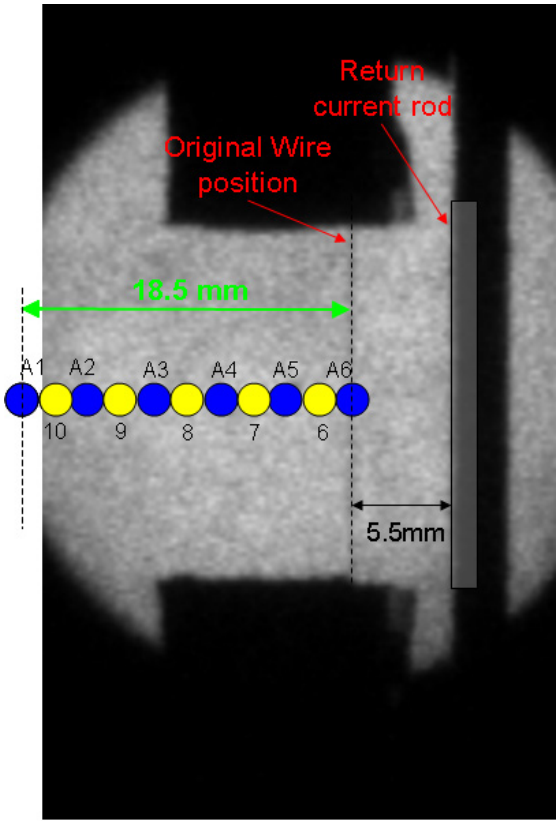

Figure 4. Position and orientation of 11x1 fiber array.

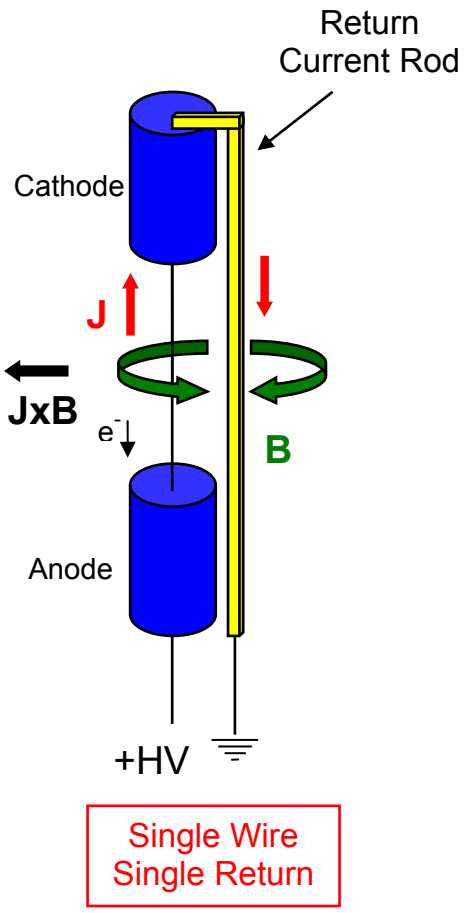

Figure 5. Schematic of single wire-single return setup.

III. Model

The basic model used to describe the wire breakdown process is that current begins to flow through the wire, resistively heating it and desorbing surface contaminant species. These species form a neutral gas cloud around the wire surface, while across the wire is a large potential. At some point, ~150ns into the current rise for our experiments, the resistance of the wire increases to a point where the current flow can not be maintained at a sufficient rate. An avalanche event occurs which rapidly breaks down the neutral gas forming a plasma. The gas is quickly ionized and expands in an adiabatic fashion away from the wire. In the case where a return current is positioned near the wire, additional JxB forces accelerate the plasma away from the wire (see Figure 5). The plasma is highly conductive and carries the bulk of the current for the remainder of the pulse. This model has been proposed and studied by various groups over the years, and provides a good qualitative picture of the breakdown process [6,7,8,9,10]. The details of this model, including various subtleties due to different wire materials, contaminants, and current drive (initial energy deposition in the wire) make this a complex problem still under investigation [11]. For our purposes, only a basic understanding is required.

IV. Results

Figure 6 shows an open shutter optical image of the wire plasma. The wire was positioned between two 12.7mm diameter stainless steel rod electrodes and held in place with a compression fit between the electrode and a tapered metal pin. The resistance across the wire was measured for each shot to maintain consistency. The wire was 20mm in length and positioned next to a solid metal return current rod. The distance from the wire to the current return could be varied, but was held at a fixed 5.5mm for shots discussed here.

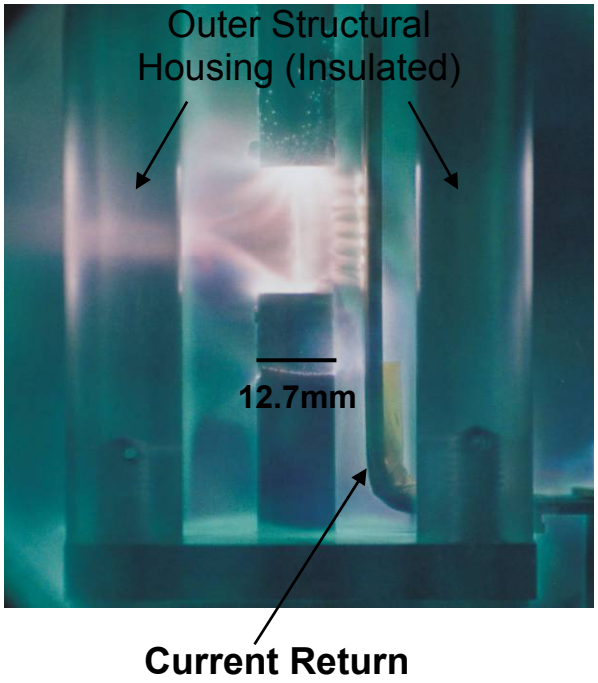

Figure 6. Open shutter visible light image of wire explosion.

For each shot, gated spectra were collected at five radial locations, identified by the yellow circles (6-10) in Figure 4. In addition, streaked spectra were collected on the farthest fiber labeled A1. The remaining fibers (A2-A6) were sent into APDs as shown in Figure 4. A sample output from the APDs for a 40kV shot (shot 121) is shown in Figure 7. Each photodetector (PD) label correlates with the fiber number (PD2 is from fiber A2). The initial spike in the waveform ~150ns correlates to the time the wire breaks down. Later in time, each photodetector increases amplitude as the plasma is propagated downstream. Note that the plasma light at any given point in time is not uniform. Variations in the emission light are present in the gated images of the plasma as well as in the spatially resolved spectral measurements shown later in this section.

Gated (3-10 ns) visible light images of the plasma evolution for different shots with 40kV charge voltages are shown in Figure 8 for several times (and different shots) relative to

the current pulse. Two ICCD cameras oriented orthogonally, imaged the plasma from the front, which shows the wire in front of the flat return current surface, and the side, which shows the side of the return current and wire. Just after the first current peak at 640ns, plasma has formed off the wire surface and has expanded radially. Note that the two brightest regions are located between the wire and return current positions on each side of the wire. Lower intensity light corresponds to plasma that is expanding due to JxB forces in the direction opposite the return current (see figure 5). By the first current zero-current crossing (870ns) the plasma has expanded farther downstream, and there is evidence of a pinched-plasma forming downstream along the center axis. By the second peak of the current, this on-axis pinched plasma has become even more pronounced. Judging from these visible light images, and the desired plasma source performance, the plasma appears to be more uniform near the first current peak. High gradients dominate the plasma after the first current zero-crossing. A more thorough investigation of the three-dimensional nature of the plasma is warranted. Based on these images, the decision was made to focus on the plasma parameters near the first zero-crossing of the current. Variations in the intensity of the plasma light at different locations and at different times are also seen in the photodetector responses shown previously (see figure 7). From just the photodetector waveforms and gated images, it is difficult to diagnose the plasma in terms of constituents and ablation rates since different species may be evolving from different areas (i.e. wire, electrodes, and kapton tape), and may be present at different locations in the plasma (see figure 19). To better diagnose the plasma, spectral measurements were performed using the two systems described earlier.

Figure 9 shows a visible light streak image for a 40kV shot (shot 121) for a 2μs record length. A pre-shot image of the wire and return current shows the orientation of the slit. The slit was located half-way between the upper and lower stainless steel electrodes holding the wire. Visible light first appears at the time the wire breaks down ~ 150ns (the same time light is first recorded by PD6, see figure 7). Note that during the first half-period of the current, the plasma is expanding in both directions. The plasma is expanding downstream (away from the return current) during the first half-period of the current at a velocity of approximately 0.6 cm/μs. At the first current zero-crossing, a bright region forms between the wire and edge of the slit. Included in this figure are the locations and timing of three of the spatially-resolved fibers (6-8) that were measured and discussed later. It is important to note the variation in intensity across the plasma varies in time as well. The Photek images (different shots) do not show light at the same location as in the visible light streak image and the APDs for the images shown in this report. Shot to shot variations in the location of the intense light regions exist. While the three-dimensional nature of the plasma is very complex, these diagnostics were useful in observing spatial phenomena in the plasma and correlating them with spectral measurements. These images also provide insight into the plasma volume at different locations and times, which is required for unfolding the spectral data to be discussed in the next section.

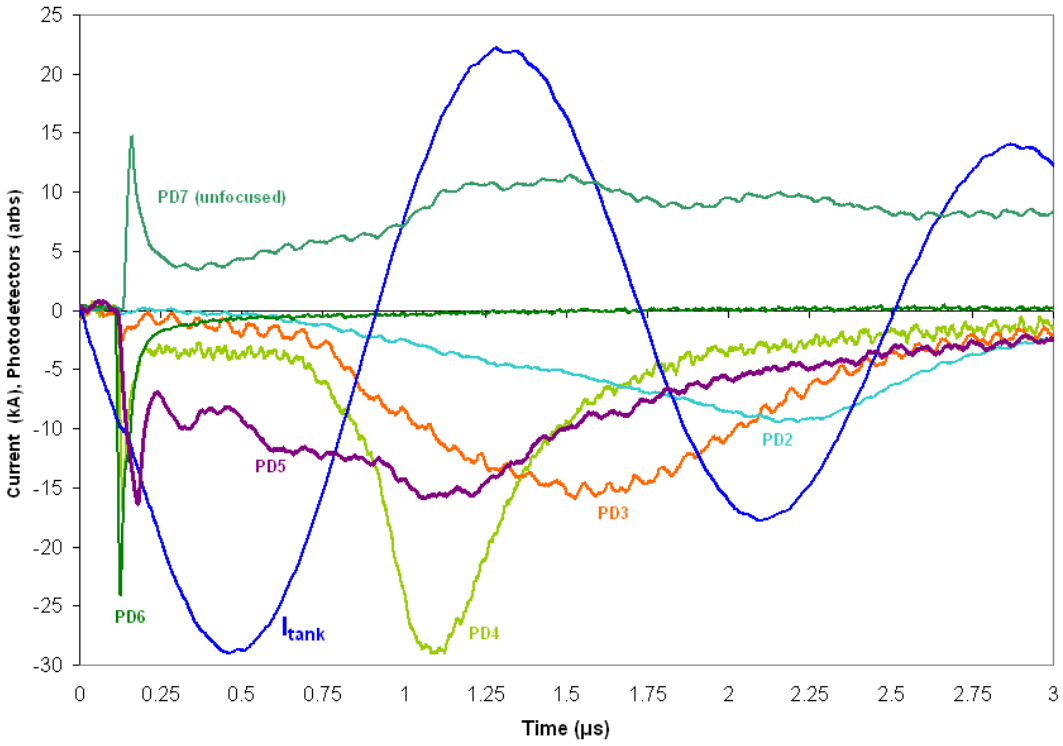

Figure 7. Output from photodetectors along with current waveform.

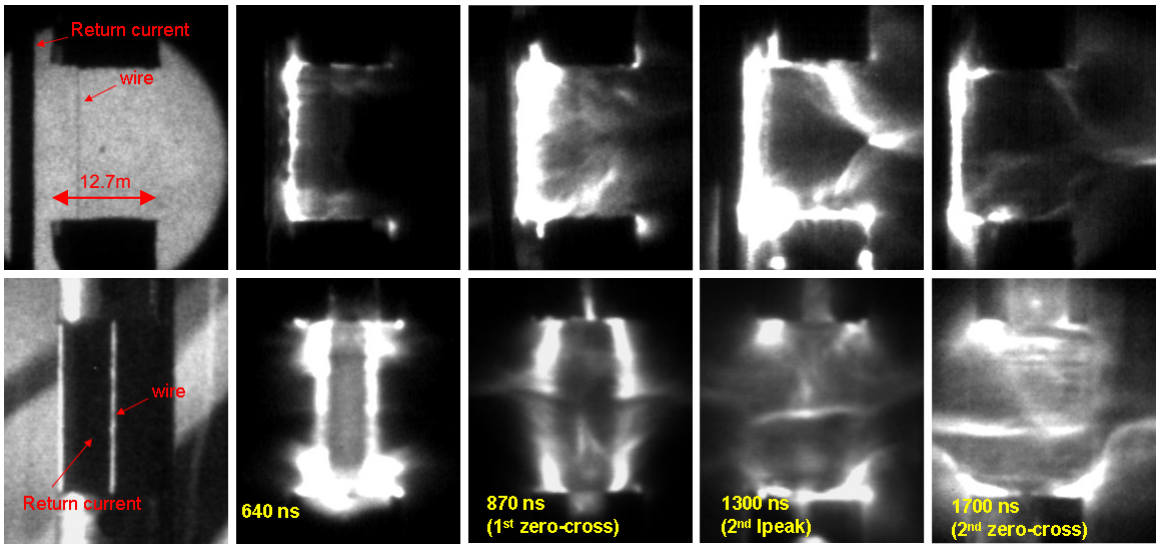

Figure 8. Side and front views of wire plasma expansion (t = 640, 870, 1300, and 1700ns).

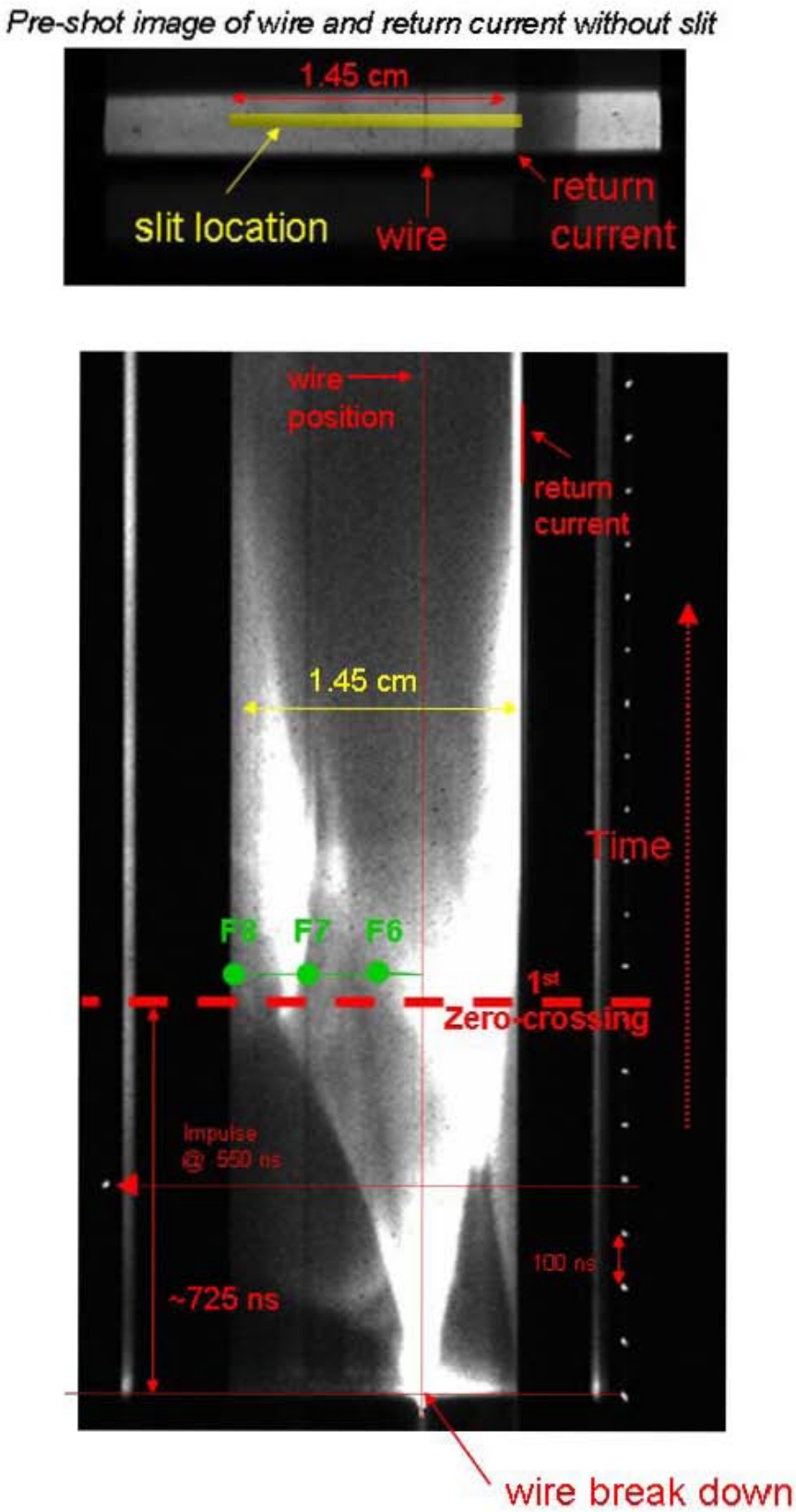

Figure 9. Visible streaked image of center cross-section of plasma. Pre-shot image shows orientation of slit, wire, and return current.

Figure 10 shows a typical spectrum for a 100μm aluminum wire. Aluminum, carbon, and hydrogen are present as neutral and low charge state ions. The aluminum is from the wire material itself, while the carbon and hydrogen are present on the surface as hydrocarbon impurities from the wire manufacturing process [12,13]. The intensities and shapes of the lines are used to determine local electron temperatures and densities, as well as ion and neutral species densities for the expanding plasma. The spectra in Figure 10 was taken with a lower resolution grating to allow for a broad wavelength range, but subsequent shots were taken using higher resolution gratings, focusing on either the H-alpha line (6563A), or the All III / Al II lines at 4480-4663A, combined with the C III / CIV lines at 4647A and 4658A. Thus two shots were required to obtain both sets of data for a particular wire configuration.

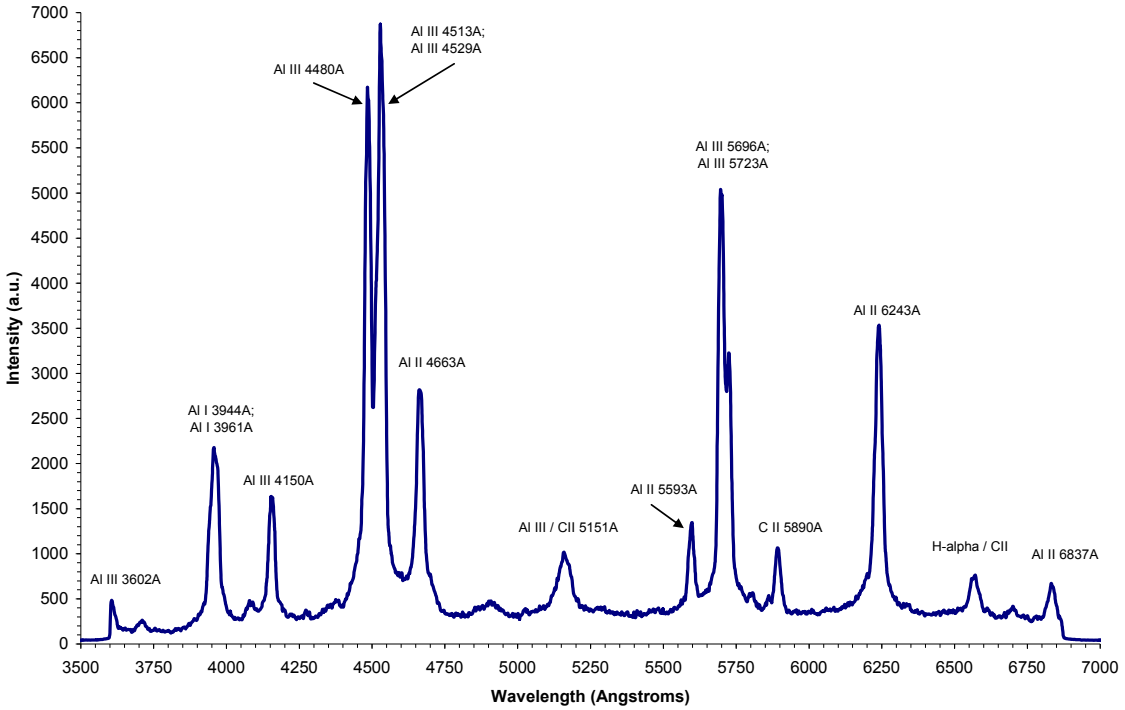

Figure 10. Typical aluminum wire discharge plasma emission spectrum.

A. Electron Density Measurements

Lineshapes were used to determine electron densities at different regions/times within the expanding plasma. In particular, the hydrogen alpha linewidth (6563Å) is subject to broadening due to micro electric fields created by electrons (and ions) in the vicinity of the hydrogen atoms [14,15]. Figure 11 illustrates this effect for fibers 6-10 collected 750ns after the initial wire breakdown during the zero-current crossing (see Figure 2) for shot 115 at 40kV charging voltage. As can be seen, the H-alpha linewidth varies across the different fibers, indicating regions of different electron density. Table 1 gives the

FWHM values for each fiber and the corresponding electron density as determined by collisional-radiative calculations [16,17].

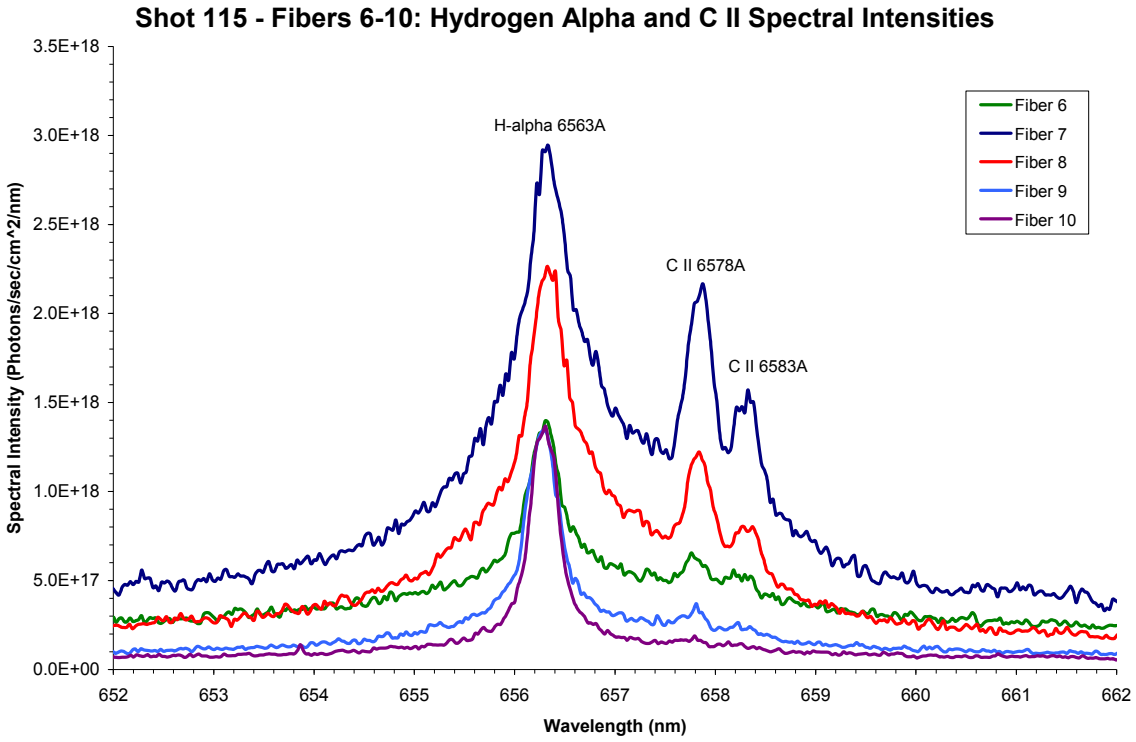

Figure 11. Hydrogen alpha and C II emission spectra.

Table 1. Electron density measurements from H-alpha linewidths.

Fiber	FWHM	Ne ($x10^{16}$ cm^{-3})
6	4.1	1.5
7	9.1	4.9
8	7.2	3.5
9	2.9	.86
10	1.8	.44

Figure 12 shows a plot of the above data along with data from two other shots at different current levels; 12.5, 29.0, and 45.0kA. While shot to shot variations occur, in general, the observed trend is that the electron density increases off the wire surface, passes

through a dense region (see streaked image in Figure 9), and steadily decreases to a level around $5x10^{15}cm^{-3}$ beyond ~13mm. It is at the farther radial distances, where the plasma parameters become more uniform, that the current can be related to density, with higher current drives generating higher densities.

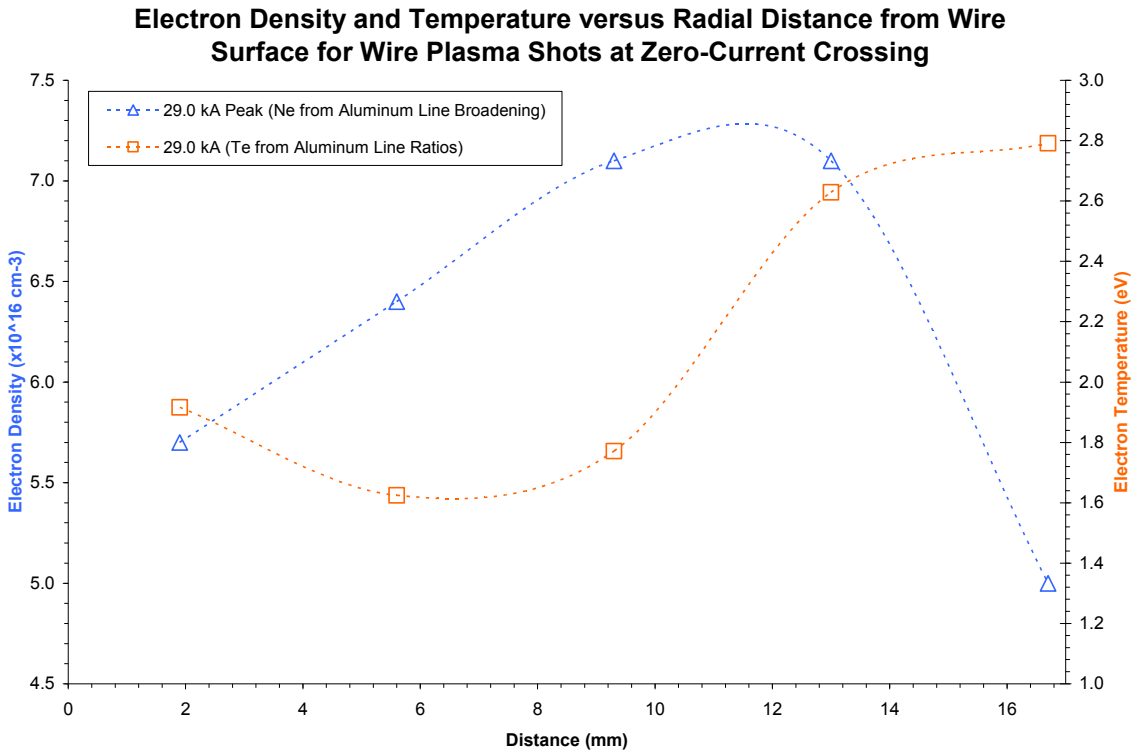

Figure 12. Electron density versus radial distance from wire.

Other lines can be Stark broadened as well [14]; however, this effect is diminished in atoms/ions with a larger number of electrons. For example, the Al III (4480Å) line (Figure 13), shows indications of Stark broadening. At these densities, the broadening is minimal, just measureable above the resolution of the instrument, but nonetheless is present and gives an additional measurement of electron density to compare with the hydrogen alpha line broadening. The calculated linewidths and densities are given in Table 2 and plotted in Figure 14. The electron density from the Al III linewidths is more constant, increasing slightly from the wire surface, before decreasing at larger distances (>13mm) approaching the values calculated from the hydrogen line. Still, the electron density from the Al III linewidths is a factor of 10 greater in the outer-most measured region. Included in this plot is the electron temperature which will be discussed in the next section.

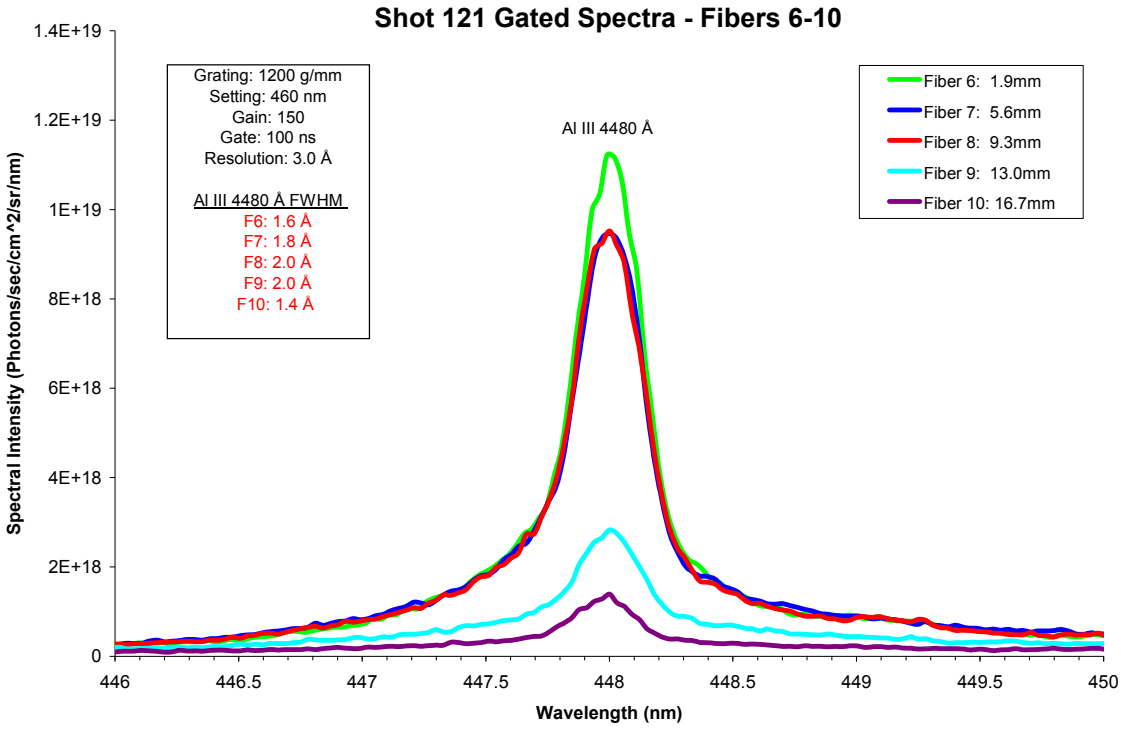

Figure 13. Al III 4480Å line intensity/width versus radial distance.

Table 2. Electron density measurements from Al III linewidths.

Fiber	FWHM	Ne ($x10^{16}$ cm^{-3})
6	1.6	5.7
7	1.8	6.4
8	2.0	7.1
9	2.0	7.1
10	1.4	5.0

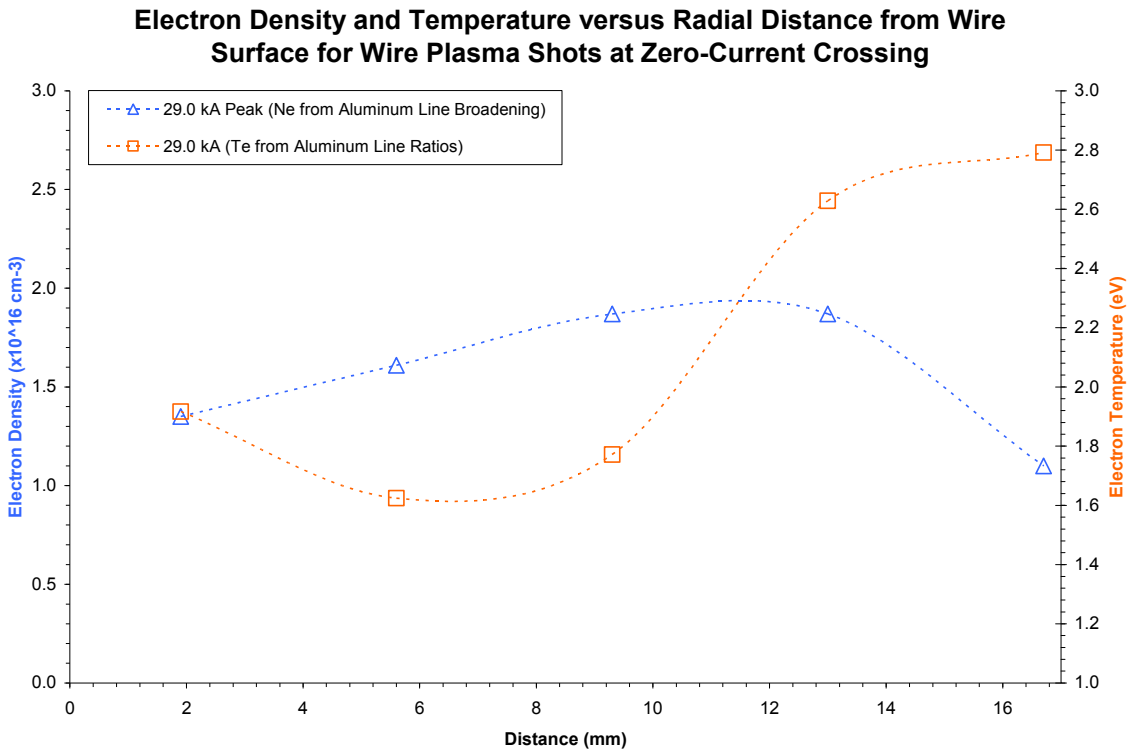

Figure 14. Electron density and temperature versus radius from aluminum line ratios and widths.

B. Electron Temperature Determinations

Electron temperature measurements of the plasma were made from line ratios using both the same and subsequent ionization states of plasma species. In particular, the ratio of the Al III 4480Å to Al III 4529Å line, and the C III 4648Å to C IV 4658Å lines were used. Using lines of different species in the plasma for temperature determinations allowed for investigations into various regions within the plasma. For two lines of the same ionization state, the following relationship can be used to determine the electron temperature [14]:

$$\frac{I_{ki}}{I_{nm}} = \frac{g_k A_{ki} \lambda_{nm}}{g_n A_{nm} \lambda_{ki}} \exp\left(\frac{-(E_k - E_n)}{kT_e}\right) \qquad (1)$$

where I is the measured integrated line intensity, A_{ki} is the Einstein coefficient for spontaneous emission, λ_{ki} is the transition wavelength, g_k is the statistical weight of the upper energy level, k is the Boltzmann constant, and E_k is the value of the upper energy level. The subscripts (k,i and n,m) refer to the upper and lower energy levels, respectively, for each transition. The transition values for the Al III lines used in this study are shown in Table 3. A plot of electron temperature versus radial distance for three shots with different current levels is shown in Figure 15.

Table 3. Transition probabilities and constants for observed Al III spectral lines.

Species	Wavelength (A)	Transition	E_i (eV) – E_k (eV)	A_{ki} (sec-1)	g_k
Al III	4479.89	$2p^6 4f - 2p^6 5g$	20.781 – 23.548		8
Al III	4479.97	$2p^6 4f - 2p^6 5g$	20.781 – 23.548		10
Al III	4528.94	$2p^6 4p - 2p^6 4d$	17.818 – 20.555	4.26×10^7	4
Al III	4529.19	$2p^6 4p - 2p^6 4d$	17.818 – 20.555	2.54×10^8	6

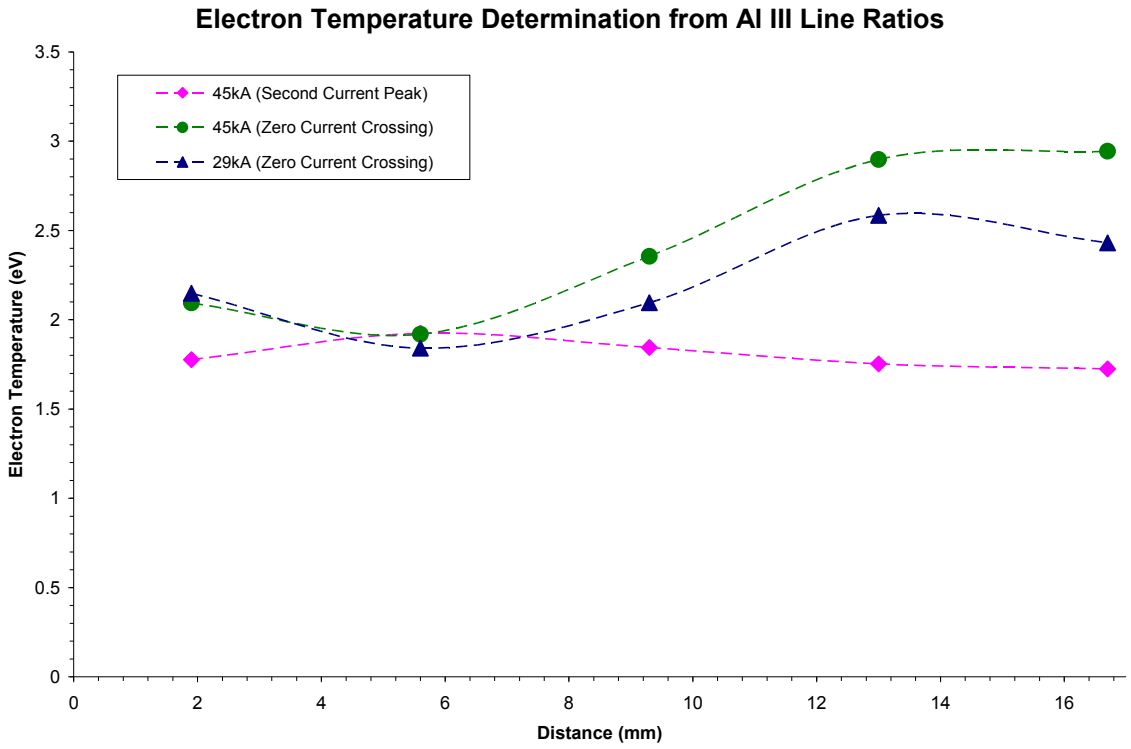

Figure 15. Electron temperature versus radial distance from Al III line ratios.

From this plot, we see that the electron temperature ranges between 1.5-3.0eV dependent on location, current, and time. For the two cases measured at the zero current-crossing time, the temperature near the wire is ~2.0 eV. The temperature then decreases slightly before beginning to increase and separate, with the higher current shot being on average about 0.3 eV or 15% higher in electron temperature. By the time of the second current

peak (400ns later), the temperature profile has become more uniform (pink waveform), and averages about 1.8 eV or 40% lower in temperature.

In addition to the Al III line ratios, electron temperatures can be determined from the subsequent ionization states of an element. The population densities of energy levels in subsequent ionization states of an element are related by the Saha equation [14]:

$$\frac{N_e N_n^z}{N_k^{z-1}} = \frac{2g_n^z}{g_k^{z-1}}\left(\frac{mkT}{2\pi\hbar^2}\right)^{\frac{3}{2}} \exp\left(\frac{-\left(E_n^z + E_\infty - E_k^{z-1} - \Delta E_\infty\right)}{kT_e}\right) \tag{2}$$

where z refers to the ionization state, z-1 the next lower ionization state, and n and k the specific quantum levels for each ionization state, respectively. E_∞ is the ionization energy and ΔE_∞ is a correction factor to the ionization energy which accounts for Coulombic interactions in the plasma. Rearranging and substituting for the integrated emission line intensity (I), the following ratio is obtained [14]:

$$\frac{I_n^z}{I_k^{z-1}} = \frac{4}{N_e}\left(\frac{m_e kT}{2\pi\hbar^2}\right)^{\frac{3}{2}} \frac{A_{nm}\lambda_{ki} g_n^z}{A_{ki}\lambda_{nm} g_k^{z-1}} \exp\left(\frac{-\left(E_n^z + E_\infty - E_k^{z-1} - \Delta E_\infty\right)}{kT_e}\right) \tag{3}$$

where n is the upper energy level of the higher ionization state and k is the upper energy level of the lower ionization state. It is this ratio, which is used to determine the electron temperature (T_e) based upon the emission intensities of two lines from subsequent ionization states of an element. Knowledge of the electron density (N_e) is required and was obtained from Stark broadening measurements of the hydrogen alpha emission line, as shown in the previous section. For the wire plasma, carbon line ratios were used to obtain electron temperatures in regions where carbon ions were present. In particular, the C III 4647A and C IV 4658A lines were used. These lines (given in Table 4) are composed of several degenerate transitions. In practice, the relative contribution for each transition to the overall line profile is calculated, and the results are compared to the experimental lineshapes. An example is shown in Figure 16 for two different electron temperatures at a constant N_e of $1x10^{16}cm^{-3}$ (reasonable for these experiments).

Table 4.Transition probabilities and constants for observed CIII and CIV spectral lines.

Species	Wavelength (A)	Transition	E_i (eV) – E_k (eV)	A_{ki} (sec-1)	g_k
C III	4647.42	$1s^2 2s3s$ – $1s^2 2s3p$	29.535 – 32.202	$7.26x10^7$	5
C III	4650.25	$1s^2 2s3s$ – $1s^2 2s3p$	29.535 – 32.200	$7.25x10^7$	3
C III	4651.47	$1s^2 2s3s$ – $1s^2 2s3p$	29.535 – 32.199	$7.24x10^7$	1
C IV	4647	$1s^2 5d$ – $1s^2 6f$	55.78-58.44	$1.85x10^8$	14

The relative contributions of each of the CIII and CIV transitions are calculated and compared with the normalized experimental line profile. As can be seen, for a given electron density the ratios of the CIII to CIV lines are highly temperature dependent. Table 5 shows the change in this ratio over a 2.0eV temperature range, assuming steady-state conditions.

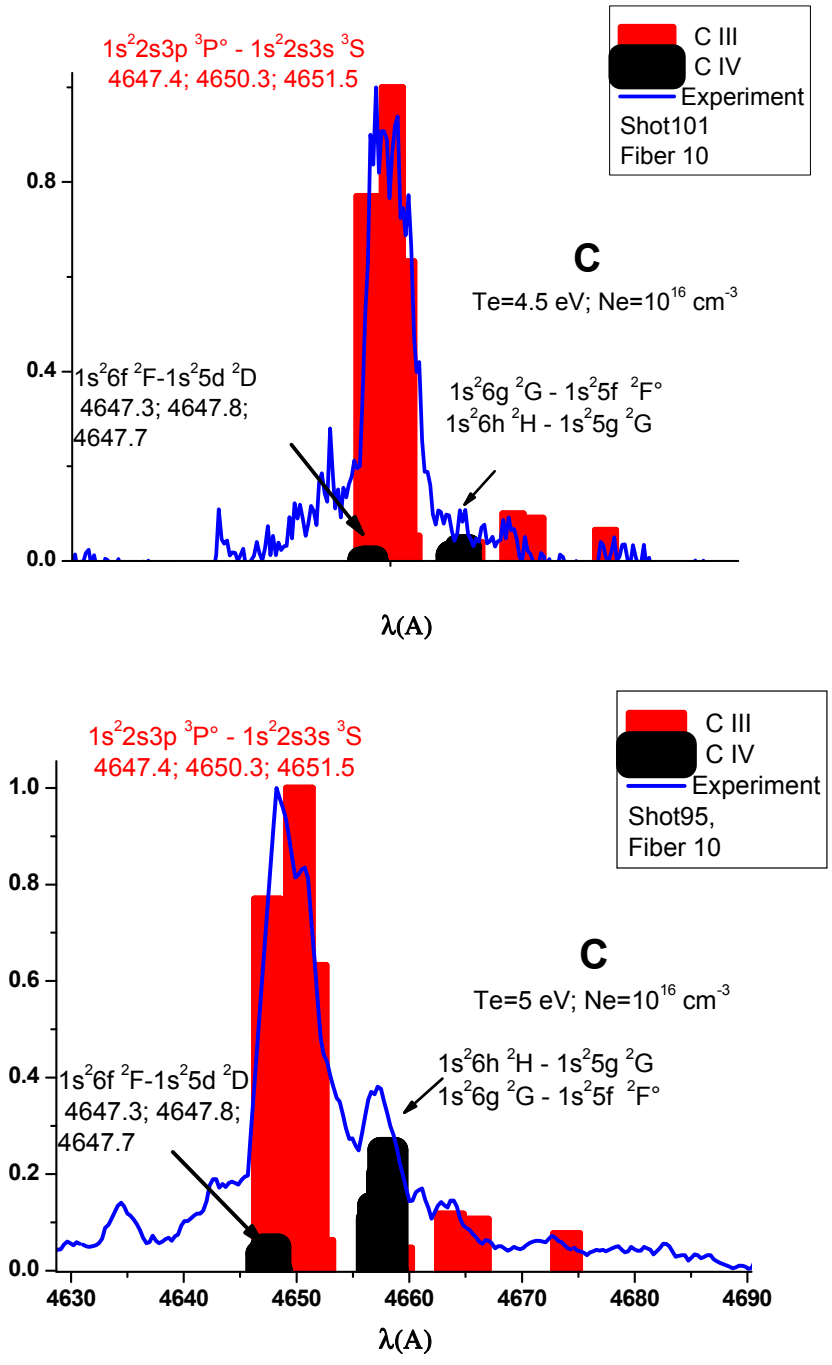

Figure 16. Fitting experimental profiles with C III / CIV lineshape calculations.

Table 5. Carbon ion line ratios versus electron temperature (T_e) at constant $N_e = 1x10^{16}$ cm^{-3}.

T_e (eV)	Ratio $I_{C\ III\ 4648}$ to $I_{C\ IV\ 4658}$
4.0	345
4.5	43.2
5.0	8.2
5.5	2.1
6.0	0.5

For the wire plasma in the outer-most region studied (18.5mm), the ratio of the CIII to CIV emission lines is close to unity, varying from 0.8 to 4.2 over a 500ns period during the rise-time of the second current peak, as shown in Figure 17.

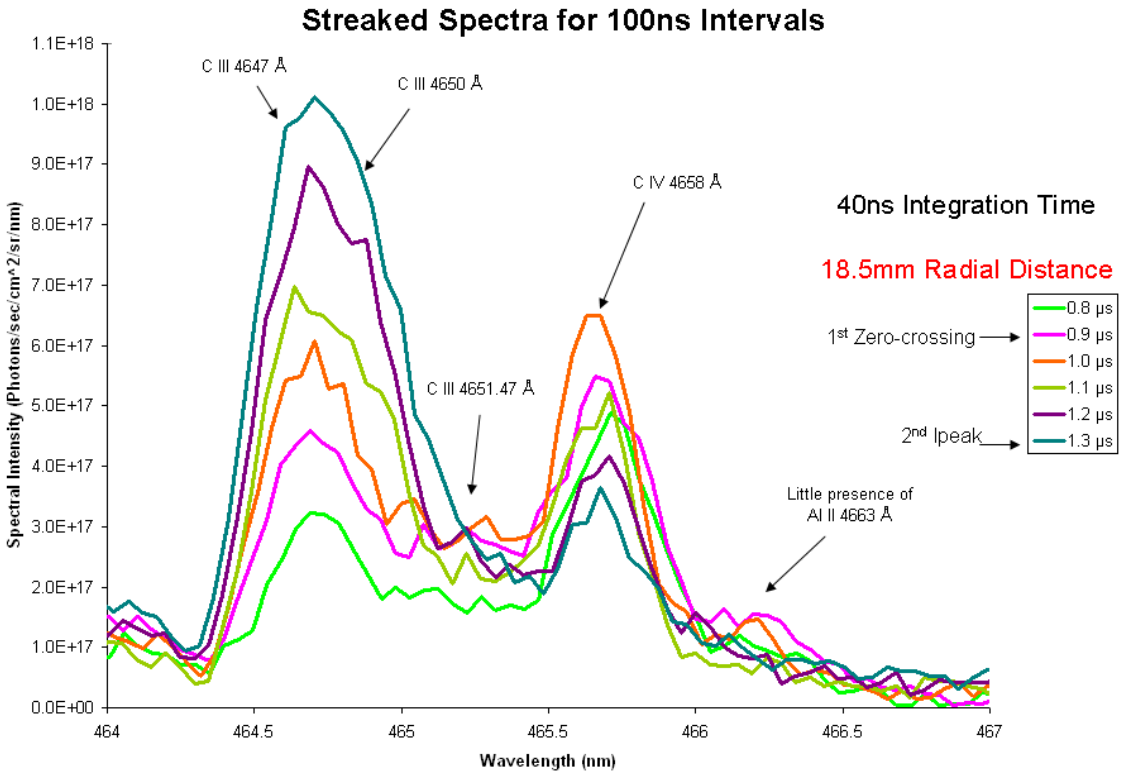

Figure 17. Streak spectra showing CIII to CIV line ratios at 100ns intervals from the first zero-crossing (0.9µs) to the second current peak (1.3µs).

Based on the line ratios from the above spectrum, the electron temperature is determined to be decreasing in time from 5.8eV to 5.2eV. Assuming steady-state conditions for this

calculation introduces an error in the T_e determination. For the CIII / CIV lines considered here, steady-state is reached in ~10μs. The CIII / CIV line ratio at steady state is ~ 4x lower than during the experiment, causing an error in the determination of T_e. However, this error is only 0.5eV (see Table 5), thus the temperatures obtained from the ratios in Table 5 need to be reduced by a factor of 0.5eV, which is done in Figure 20. For comparison, the Al III line ratios (Figure 18) over this same period show the temperature to be decreasing from 3.0eV to 2.4eV.

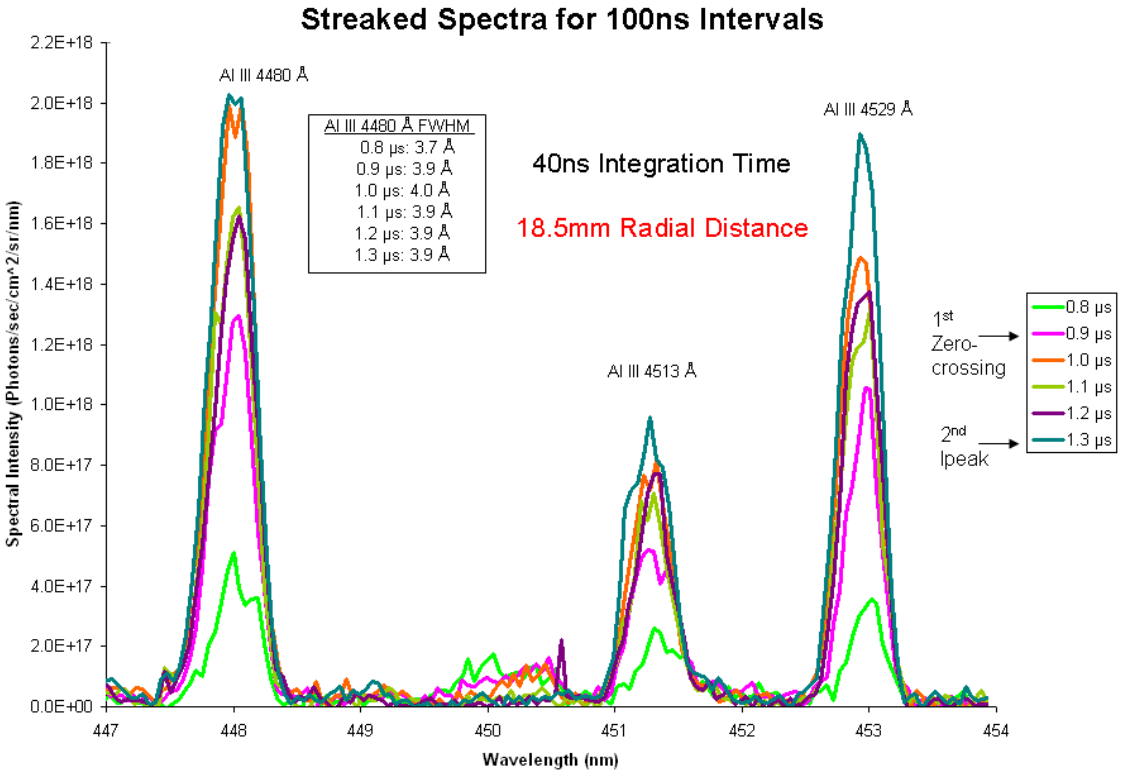

Figure 18. Streak spectra showing Al III 4480Å to 4529Å line ratios at 100ns intervals from the first zero-crossing (0.9μs) to the second current peak (1.3μs).

In general, there is a factor of two variation in the electron temperature between the carbon and aluminum line ratios, consistent with the idea of there being a lower density outer plasma region composed of primarily hydrocarbon plasma with a cooler, higher density aluminum plasma center, as illustrated in Figure 19. Figure 20 shows the radial variation in electron temperature determined from carbon ion line ratios along with the corresponding electron densities from hydrogen line broadening. These data were taken at the zero-current crossing and corresponds to the 0.9μs time in the previous figures. As was the case in Figure 14, the electron density decreases at increased radius, while the electron temperature increases, and we again find a relatively stable region at distances greater than 13mm where the electron density is ~$5x10^{15}cm^{-3}$ and the electron temperature is ~5.3eV.

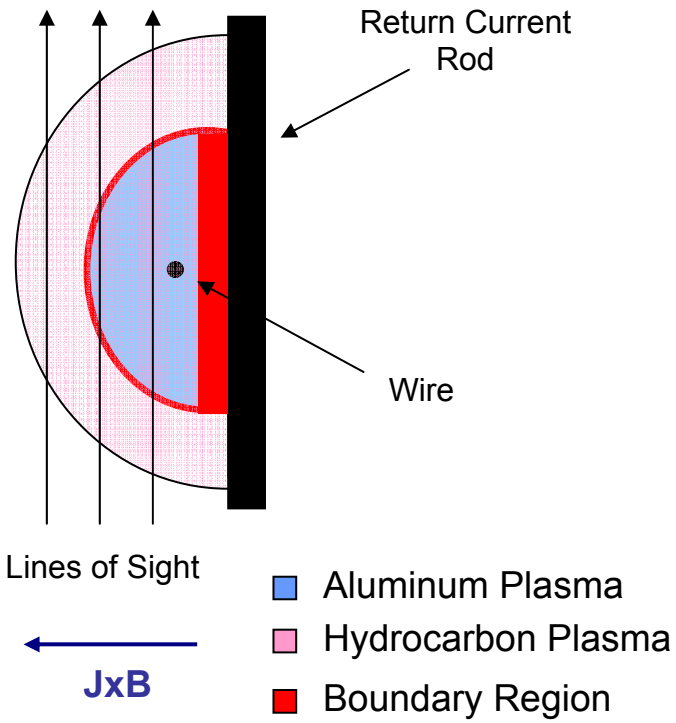

Figure 19. Illustration of plasma regions and spectroscopic lines of sight.

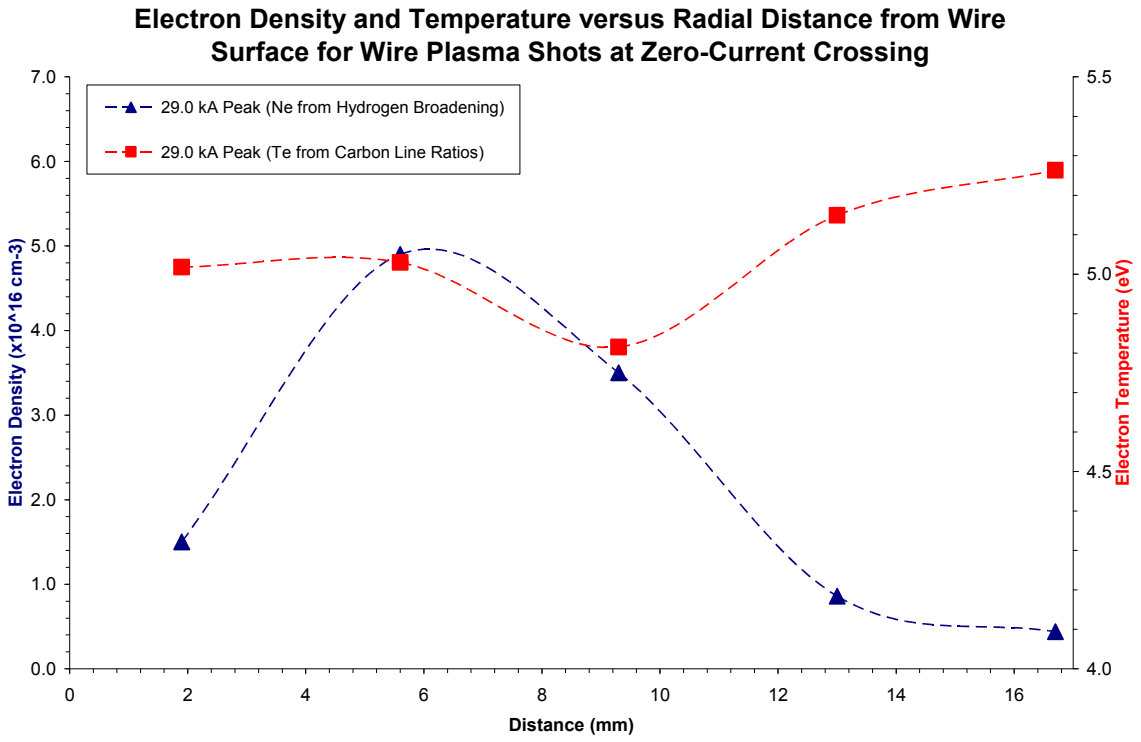

Figure 20. Electron density and temperature versus radial distance.

C. Absolute Line Intensities

Finally, some discussion should be made regarding absolute line intensities. All of the spectra shown in the previous figures were calibrated using known spectral lamp sources. This allowed the intensity measurements from the detectors to be converted to photon radiance of the source (photons/second/steradian/cm^2). Knowing this radiance, the number density of individual species can be determined and compared with calculated values based on measured electron densities and temperatures [18]. Calculations were performed for both hydrogen neutral and aluminum doubly ionized lines, for both steady-state and time-dependent cases. Further discussion regarding the details of these calculations will be made in a subsequent report; this report only focuses on the steady-state calculations. Using the electron density determined from Stark broadening of the hydrogen alpha line and the electron temperature obtained from carbon ion line ratios, the total hydrogen alpha line intensity can be calculated for a specific concentration of neutral hydrogen atoms. For this calculation, steady-state is assumed and the electron density is set equal to the ion (proton) density (conditions similar to those in the outer-most fiber region). There are time dependencies for the level populations and ionization/recombination times, and these have been calculated for the time-scales of this experiment (100's of nanoseconds). These time dependencies introduce small correction factors to the steady-state calculations, which will be neglected for the purpose of this report. Table 6 shows the results for the case of neutral hydrogen at two temperatures with $N_i = 1x10^{16}$ cm^{-3} and a plasma length of 1.5cm. Table 7 shows the same calculations for a factor of three increase in total ion density.

Table 6. Steady-state calculations of hydrogen alpha line intensity, $N_i = 1x10^{16}$ cm^{-3}.

T_e (eV)	N_e (cm^{-3})	N_H (cm^{-3})	τ	Intensity (photons/sec/ster/cm^2)
3	$9.91x10^{15}$	$9x10^{13}$	.02	$9.8x10^{17}$
5	$9.94x10^{15}$	$6x10^{13}$	.004	$3.7x10^{17}$

Table 7. Steady-state calculations of hydrogen alpha line intensity, $N_i = 3.1x10^{16}$ cm^{-3}.

T_e (eV)	N_e (cm^{-3})	N_H (cm^{-3})	τ	Intensity (photons/sec/ster/cm^2)
3	$3.06x10^{16}$	$4x10^{14}$	.2	$8.9x10^{18}$
5	$3.08x10^{16}$	$2x10^{14}$	.03	$3.5x10^{18}$

Comparing this to the intensities measured for shot 115 at the relevant temperatures and densities, we see that an order of magnitude increase in intensity (highlighted) gives a factor of 6.7 increase in neutral hydrogen density. Total line intensities for hydrogen from the experimental data range from 5.4×10^{17} to 2.7×10^{18} photons/sec/ster/cm^2, and thus fall within this region, giving neutral hydrogen densities of between 2×10^{14} cm^{-3} and 6×10^{13} cm^{-3}. Further computations are being carried out to improve the precision of these values; however, it is clear that most of the hydrogen is ionized and the overall neutral population is low.

Similar calculations were performed for the Al III line intensities at 4480Å. Table 8 shows the results of one such calculation, with an electron density of 3×10^{16} cm^{-3} and a total aluminum fraction of 10% (similar to that expected in the outer fiber regions). From these calculations, we see that the Al III species densities are in the low 10^{14} cm^{-3} ranges.

Table 8. Steady-state calculations of Al III (4480Å) line intensity, $N_i = 3 \times 10^{16}$ cm^{-3}.

T_e (eV)	N_e (cm^{-3})	$N_{Al\ III}$ (cm^{-3})	τ	Intensity (photons/sec/ster/cm^2)
3	3.0×10^{16}	3.0×10^{14}	.96	1.2×10^{19}
5	3.0×10^{16}	1.3×10^{14}	.07	2.4×10^{18}

IV. Conclusions

A series of experiments were conducted to investigate plasma formation and propagation from exploding wires. A high voltage, capacitive discharge was driven through a 100μm diameter aluminum wire to form a plasma. The plasma was composed of hydrocarbon and pure metal species of low charge states (singly and doubly ionized). Electron temperatures and densities were measured using spectroscopic techniques, such as line broadening and intensity ratios. Both temporal and spatial measurements were taken which showed variations in density and temperature profiles within the plasma and between constituent species. Hydrogen and carbon were shown to expand at a greater rate (5.2 cm/μs and 4.4 cm/μs, respectively) and with a higher electron temperature and lower density than aluminum Al III species (2.6 cm/μs). Density and temperatures variations were observed extending radially from the wire surface. At large radial distances (>13mm) these variations decreased and the plasma parameters became more stable. It is this outer region which is of interest to the radiography program, since larger plasma volumes (a few cm^3) are desired for applications such as intense electron beam propagation and focusing. These experiments were taken utilizing a single wire with a single return current post positioned a few millimeters away from the wire. Such a configuration allowed for additional JxB forces to accelerate ions in the plasma away

from the wire. This acceleration was observed in both the optical images and measured line spectra. Some control over the plasma parameters (N_e, T_e) was observed with changes in current drive and geometry. It is expected that similar control can be achieved through manipulation of the wire material and thickness. While this research focused on aluminum wire and aluminum plasmas, early on it became evident that hydrocarbon plasmas of significant densities were formed as well. These plasmas, originating from surface contaminants on the wire, expand more quickly and cover a greater volume than the aluminum plasma on the same timescale. The hydrogen and carbon species are low mass and their atomic physics is well understood, making them useful both as a practical source and for plasma modeling. This opens up the possibility of using alternative materials and/or thicknesses of wire to obtain greater hydrocarbon species with less metal material. In particular, earlier experiments conducted at the University of Michigan [13] on a single wire setup at lower currents showed that a hydrocarbon plasma (with similar parameters to those reported here) could be generated from a tungsten wire without vaporizing the wire, thus eliminating altogether the metal species from the plasma. Similarly, a larger diameter wire could be used providing more surface area for contaminants. Overall, these experiments demonstrated that a plasma can be formed with slowly varying parameters (over 100's of nanoseconds) over relatively large distances of interest for electron beam transport. More work is needed to fully understand the dynamics of the plasma and issues regarding spatial variations and shot reproducibility. Nevertheless, we were successful at creating a plasma in the 10^{16} cm^{-3} density regime with electron temperatures of a few eV which was original stated purpose of this work.

References

[1] D.R. Welch et al., "Transport of a Relativistic Electron Beam in Gas and Plasma-Filled Focusing Cells for X-ray Radiography," Physics of Plasmas, 11**,** 751 (2002).

[2] K. Hahn, "Electron Beam Focusing in Gas and Plasma-Filled Transport Cells," Ph.D. Dissertation, University of New Mexico (2006).

[3] B.V. Oliver, D. Short, G. Cooper, J. McLean, and J. O'Malley, "Paraxial Gas-Cell Focusing of Relativistic Electron Beams for Radiography," IEEE Transactions on Plasma Sci. 33, 704 (2005).

[4] V.V. Alexandrov, A.V. Branitskii, G.S. Volkov, *et al*., "Dynamics of Heterogeneous Liners with Prolonged Plasma Creation," Plasma Phys. Reps. 27, 89 (2001).

[5] E.P. Yu, B.V. Oliver, P.V. Sasorov, *et al*., "Steady-State Radiation Ablation in the Wire-Array Z-Pinch," Physics of Plasmas, 14, 022705 (2007).

[6] K.M. Chandler, D.A. Hammer, D.B. Sinars, S.A. Pikuz, and T.A. Shelkovenko, "The Relationship Between Exploding Wire Expansion Rates and Wire Material Properties Near the Boiling Temperature," IEEE Transactions on Plasma Science, 30, 577 (2002).

[7] J.P. Chittenden, S.V. Lebedev, J. Ruiz-Camacho, F.N. Beg, S.N. Bland, *et al*., "Plasma Formation in Metallic Wire Z-Pinches," Physical Review E, 61, 4370 (2000).

[8] P.U. Duselis and B.R. Kusse, "Experimental Observation of Plasma Formation and Current Transfer in Fine Wire Expansion Experiments," Physics of Plasmas, 10, 565 (2003).

[9] G.S. Sarkisov and D. McCrorey, "Imaging of Exploding Wire Phenomena," IEEE Transactions on Plasma Science, 30, 98 (2002).

[10] D.B. Sinars, T.A. Shelkovenko, S.A.Pikuz, J.B. Greenly, and D.A. Hammer, "Exploding Aluminum Wire Expansion Rate with 1-4.5 kA per Wire," Physics of Plasmas, 7, 1555 (2000).

[11] G.S. Sarkisov, S.E. Rosenthal, and K.W. Struve, "Thermodynamical Calculation of Metal Heating in Nanosecond Exploding Wire and Foil Experiments," Review of Scientific Instruments, 78, 043505 (2007).

[12] E. Lassner and W.D. Schubert, Tungsten: Properties, Chemistry, Technology of the Element, Alloys, and Chemical Compounds, Kluwer Academic/Plenum Publishers, New York (1999).

[13] M.D. Johnston, "Ionization Dynamics of a Single Wire Z-Pinch," Ph.D. Dissertation, University of Michigan (2004).

[14] H.R. Griem, Plasma Spectroscopy, McGraw Hill, New York (1964).

[15] H.R. Griem, Spectral Line Broadening by Plasmas, Academic Press, New York (1974).

[16] E. Stambulchik and Y. Maron, "A Study of Ion-Dynamics and Correlation Effects for Spectral Line Broadening in Plasma: K-shell Lines," Journal of Quantitative Spectroscopy & Radiative Transfer, 99, 730 (2006).

[17] E. Stambulchik and Y. Maron, "Stark Effect in High-n Hydrogen-like Transitions," Journal of Physics B. 41, 095703 (2008).

[18] Yuri V. Ralchenko and Y. Maron, "Accelerated Recombination Due to Resonant Deexcitation of Metastable States," Journal of Quantitative Spectrscopy & Radiative Transfer, 71, 609 (2001).

Distribution:

2	Voss Scientific Attn: D. R. Welch D. V. Rose 418 Washington St. SE Albuquerque, NM 87108	
1	Dept. of Electrical & Computer Engineering Attn: Edl Schamiloglu MSC01 1100 1 University of New Mexico Albuquerque, NM 87131-001	
5	MS 1195	M. D. Johnston
5	MS 1195	K. D. Hahn
3	MS 1195	B. V. Oliver
1	MS 1181	T. A. Mehlhorn
1	MS 1195	S. R. Cordova
1	MS 1195	I. Molina
1	MS 1195	B. Bui
1	MS 1195	J. J. Leckbee
1	MS 1193	D. W. Droemer
1	MS 1193	M. D. Crain
1	MS 1193	M. E. Cuneo
1	MS 1193	D. C. Rovang
1	MS 1194	J. R. Woodworth
1	MS 1196	J. E. Bailey
1	MS 1423	P. A. Miller
1	MS 0123	D. Chavez, LDRD Office, 1011
1	MS 9536	Technical Library (electronic copy)


Sandia National Laboratories